A joint image encryption based on a memristive Rulkov neuron with controllable multistability and compressive sensing

Yongxin Li[1, 2], Chunbiao Li[1, 2 a)], Yaning Li[3], Irene Moroz[4], Yong Yang[5]

[1]*School of Electronic and Information Engineering, Nanjing University of Information Science & Technology, Nanjing 210044, China*

[2]*School of Artificial Intelligence, Nanjing University of Information Science & Technology, Nanjing 210044, China*

[3]*School of Electrical & Electronic Engineering, University College Dublin, Dublin D04V1W8, Ireland*

[4]*Mathematical Institute, University of Oxford, Oxford OX2 6GG, UK*

[5]*RISC-V Research Institute, Nanjing Qinheng Microelectronics Co., Ltd*

ABSTRACT

Image encryption, as a critical branch, has attracted increasing attention to the demand for information security specifically in the era of artificial intelligence (AI). A chaotic sequence is regarded as an important encryption source, and compressive sensing provides an effective technology for obtaining and reconstructing sparse or compressible signals in applied electronic engineering. In this work, the detouring matching pursuit algorithm and DNA coding are utilized to increase the performance based on a newly developed chaotic firing neuron. A memristor as the electromagnetic component is proven to enhance synaptic plasticity and emulate the synaptic connections in the brain. A unique discrete memristive neuron is derived for exploring the dynamics of neuron firing. By modifying the feedback from the memristor various coexisting neuronal chaotic firing are possessed. Because of the periodic evolution of the resistor from the memristor, the derived memristive Rulkov neuron exhibits coexisting homogeneous and heterogeneous multistability, which enables amplitude controllability and different types of coexisting chaotic firings. Circuit implementation based on CH32 is built to verify the controllability of the coexisting dynamics.

Keywords: Rulkov neuron, discrete memristor, firing multistability, image encryption.

---

a) Corresponding author. E-mail address: goontry@126.com; chunbiaolee@nuist.edu.cn

1. Introduction

Image encryption has attracted increasing attention in the rapid development of information security, where sensitive information is protected from unauthorized access [1-2]. At the same time, compressive sensing has also been widely applied in electronic engineering since the sparse signals may reduce the burden of image storage and transmission [3-4]. With the exponential growth of genetic and biometric data, the protection of data associated with healthcare, genetics, and personalized medicine has encountered greater challenges. DNA encryption provides a cutting-edge solution to protect the confidentiality and integrity of genetic profiles, mitigating the potential risks associated with data breaches. The mathematical modeling of chaotic neurons could also contribute to data security. Recently, different types of neurons have been found to exhibit chaos [5-7]. The famous Hodgkin-Huxley (HH) neuron based on physiological experiments was first proposed in 1952 [8-9]. In 1961, the FitzHugh-Nagumo (FHN) neuron in two dimensions was obtained, inspired by the Van der Pol equation [10-11]. All these neuronal models can be employed to chaos generate when new nonlinearities are introduced.

One such popular nonlinear unit in the field of neuroscience is the memristor [12] synapse. When the first physical memristor was developed in 2008, research on memristors became more active [13]. Since then, the memristor has been the subject of intensive research because of its potential applications to neuromorphic computing [14-15]. The Hopfield neural network is equipped with two memristive synaptic weights to achieve offset control. The memristive neural network with self-reproducing attractors is formed by combining two sub-neural networks and one multistable memristor synapse. Furthermore, the flux-controlled locally active memristor provides a new technology for generating abundant hidden firing and moving attractors to any desired location by offset boosting [16]. Discrete memristor has attracted wide attention in recent years. Bao et al. designed a class of novel discrete memristors and explored their application in secure communication [17-18]. Furthermore, discrete memristive neurons show similar dynamics, and for this reason, they have attracted increasing interest in the nonlinear field. Magnetic induction effects were emulated by the memristive Rulkov neuron in [19]. The locally active discrete memristor was utilized to couple two Rulkov neurons to regulate brain-like dynamics [20]. However, there is

much margin in the study of discrete maps, especially since the phenomenon of firing multistability has not been well studied in discrete memristive neurons.

The objectives of this paper are highlighted as follows:

(1) The cross-research of information security and neuroscience is exemplified in the memristive neuron combined with the DNA encoding for image encryption.

(2) A low-complexity, high-accuracy greedy algorithm known as Detouring Matching Pursuit (DMP) is applied for the reconstruction of sparse signals. The exploration of homogeneous and heterogeneous multistability is discussed with the integration of DNA coding technology.

(3) An elegant memristive Rulkov neuron is constructed to exhibit complex chaotic dynamics. The various firing patterns are modified by the feedback strength and initial conditions of memristors, including periodic spiking, periodic bursting, chaotic spiking, and chaotic bursting activities.

(4) The coexisting attractors are flexibly extracted by proper initial conditions by the parameters of the memristor. Homogeneous and heterogeneous multistability are captured in the derived system.

(5) The digital circuit is built based on CH32 and the experimental results, shown in the oscilloscope, agree with numerical simulations and theoretical predictions.

The remainder of this paper is organized as follows: In Section 2, the memristive Rulkov neuron is established, and the typical firing activities are given along with the basic dynamical analysis. In Section 3, the CH32-based digital circuit platform is carried out to verify numerical simulation. In Section 4, the image encryption algorithm based on DMP and DNA coding is implemented to explore the influence of coexisting chaos. The last section contains conclusions.

2. A 3D memristive Rulkov neuron and dynamical analysis

2.1 Discrete memristor

The constitutive relation of the memristor, as expressed in a continuous system, can be transformed into a discrete map via the Euler method [19-20]:

$$\begin{cases} v_n = M(q_n) i_n = \cos(q_n) i_n, \\ q_{n+1} = q_n + 0.01 i_n, \end{cases} \tag{1}$$

The current $i(t)$, voltage $v(t)$, and $q(t)$ in continuous time here are denoted by i_n, v_n, and q_n in Eq. (1). In the MATLAB simulation platform, the memristor input is set as the discrete sinusoidal current $i_n = H\sin(\omega_n)$. The fingerprints of the discrete memristor are shown in Fig. 1(a), when $\omega = 0.02$, $q_0 = 0.1$, $H = 1.0$, $H = 1.2$, and $H = 1.4$. Figure. 1(b) shows frequency-related fingerprints by fixing $H = 1.5$, $q_0 = 0.1$, and $\omega = 0.02$, $\omega = 0.03$, $\omega = 0.04$.

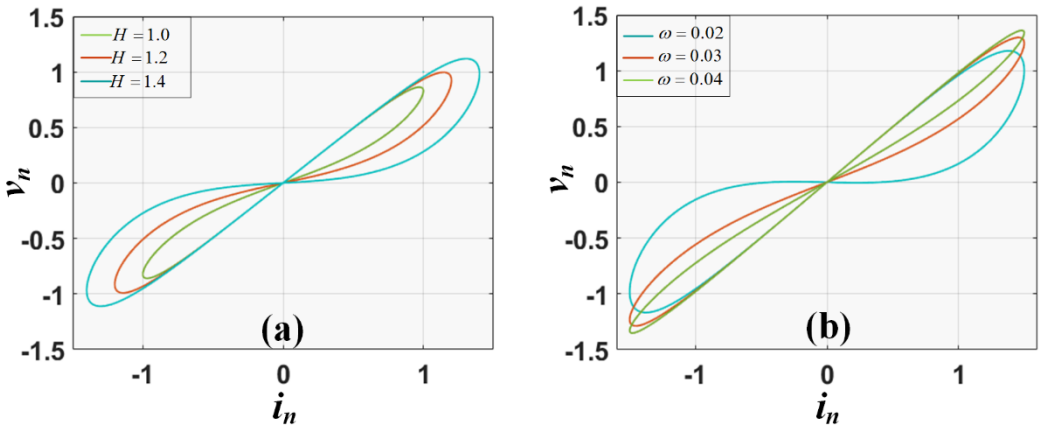

Fig. 1. The fingerprints of discrete memristor with $q_0 = 0.1$: (a) set $\omega = 0.02$, and $H = 1.0$, $H = 1.2$, $H = 1.4$, (b) when $H = 1.5$, and $\omega = 0.02$, $\omega = 0.03$, $\omega = 0.04$.

2.2 Memristive neuron system

Based on the ideas from the memristive Rulkov maps [21-23],

$$\begin{cases} x_{n+1} = \dfrac{a}{1+x_n^2} + y_n + b\cos(dz_n + e)x_n \\ y_{n+1} = y_n + cx_n \\ z_{n+1} = z_n + 0.01x_n, \end{cases} \tag{2}$$

here x_n, y_n, and z_n represent the n-th iterate of the map (2). There is a direct transformation from the cosine function to the sine function, which is associated with the frequency and initial phase. For disclosing more possible dynamics, here three parameters b, d, and e are employed for comprehensive analysis. The number of iterations used for the plots of bifurcation and Lyapunov exponents are 60000 and 3000, respectively. As shown in Fig. 2(a)(b), when the frequency increases to a certain value of about 100, the map exhibits robust hyperchaos. The initial phase poses periodic modulation connected by periodic windows, as indicated by Fig.2(c)(d). The case when

$d = 1$, $e = 0$ shows almost the same dynamics as the system proposed in [23]. When the frequency parameter d increases in the periodic function, robust hyperchaos with almost linearly increased Lyapunov exponents is observed. Typical dynamics of map (2) are summarized in Table 1 and corresponding neuronal behaviors are illustrated in Fig. 3. In the following, we focus on the case of map (2) with $a = 8$, $b = 0.1$, $c = –0.4$ for further observation.

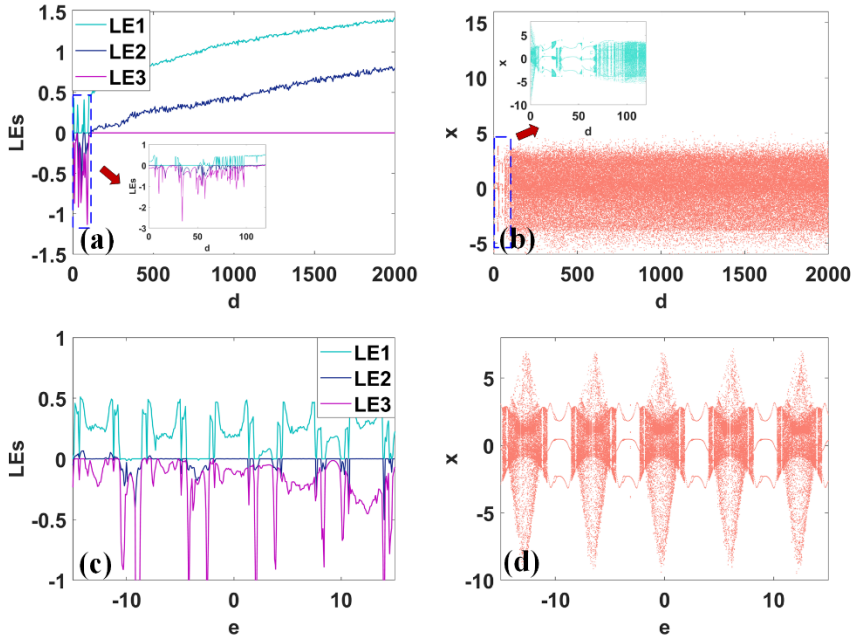

Fig. 2. Dynamical evolution of the system (2) according to the frequency parameter d and amplitude parameter e when $(x_0, y_0, z_0) = (1, 0, 0)$ and $a = 5$, $b = 0.8$, $c = –0.1$, where (a) and (c) are Lyapunov exponents, (b) and (d) are bifurcation diagrams: (a)-(b) $e = 0$, d varies in [0, 2000], (c)-(d) $d = 1$, e varies in [-15, 15].

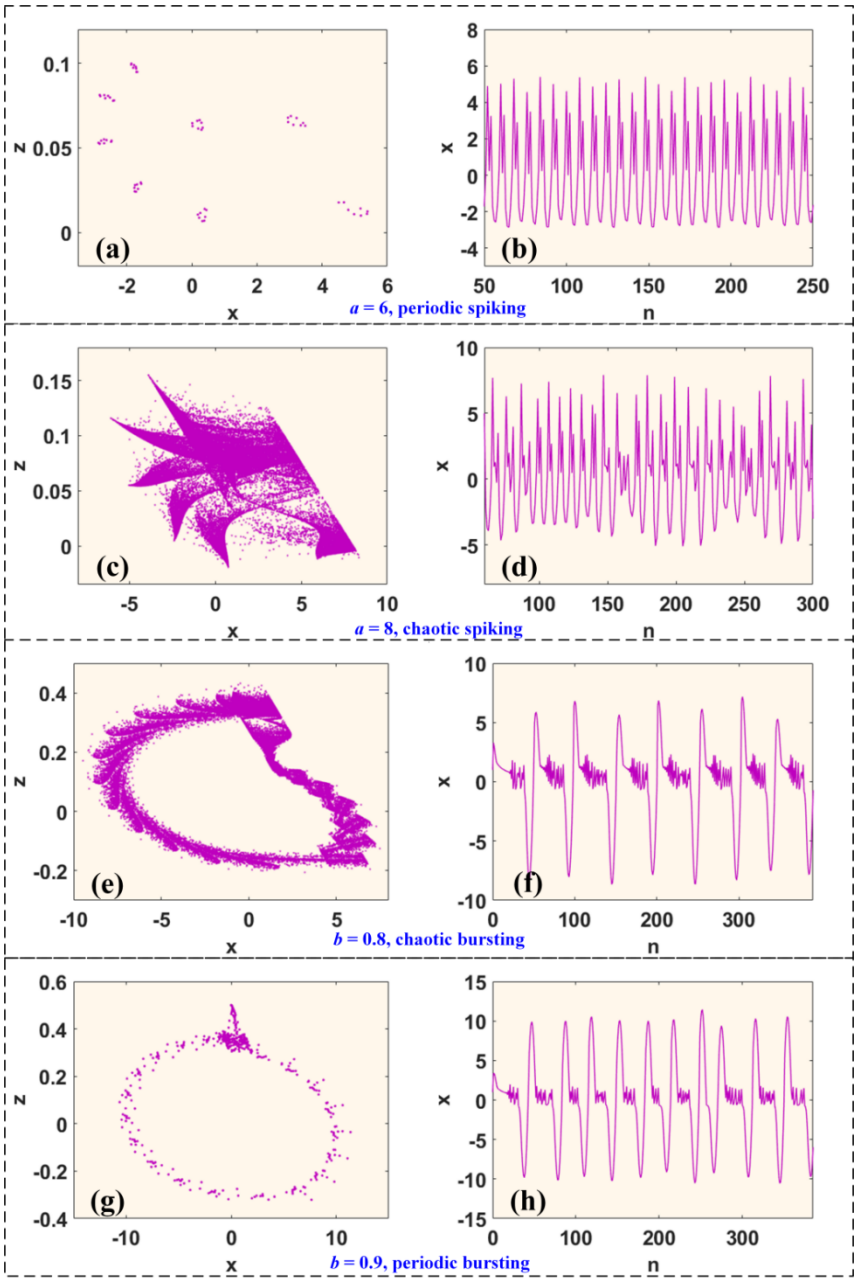

Fig. 3. Typical firings of the map (2) with $(x_0, y_0, z_0) = (1, 0, 0)$: (a)-(b) periodic spiking when $a = 6$, $b = 0.1$, $c = -0.4$, (c)-(d) chaotic spiking when $a = 8$, $b = 0.1$, $c = -0.4$, (e)-(f) chaotic bursting when $a = 5$, $b = 0.8$, $c = -0.1$, (g)-(h) periodic bursting when $a = 5$, $b = 0.9$, $c = -0.1$.

Table 1. Typical dynamics of the map (2) with $(x_0, y_0, z_0) = (1, 0, 0)$.

Parameter	Attractor type	Lyapunov exponents
	I: $b = 0.1$, $c = -0.4$	
$a = 6.0$	Periodic points	0, –0.004, –0.025
$a = 8.0$	Chaos	0.2581, 0, –0.02
	II: $a = 5$, $c = -0.1$	
$b = 0.8$	Chaos	0.1802, 0, –0.1286

$b = 0.9$	Chaos	0.0869, –0.021, –0.061

2.2 Firing multistability analysis

The Rulkov neuron is equipped with a discrete memristor for its unique function in synaptic plasticity. Due to the memory effect of the memristor, the coexisting multistable firing, found in the map-based neuron, shows complex brain-like dynamics. When $a = 8$, $b = 0.1$, $c = –0.4$ under $(x_0, y_0, z_0) = (1, 0, z_0)$, the feature of firing multistability is shown in Fig. 4, where the coexistence of homogeneous and heterogeneous multistability is revealed. This coexisting multistable firing is plotted in Fig. 5. Further simulation revealed that for $a = 5$, $b = 0.9$, $c = –0.1$, the amplitude-frequency of firing activities are regulated by y_0, as illustrated in Fig. 6. When $a = 5$, $b = 0.9$, $c = –0.1$ and y_0, z_0 varies in [–12.5, 12.5], the 2D Lyapunov exponents and sample entropy of the map (2) are plotted in Fig. 7.

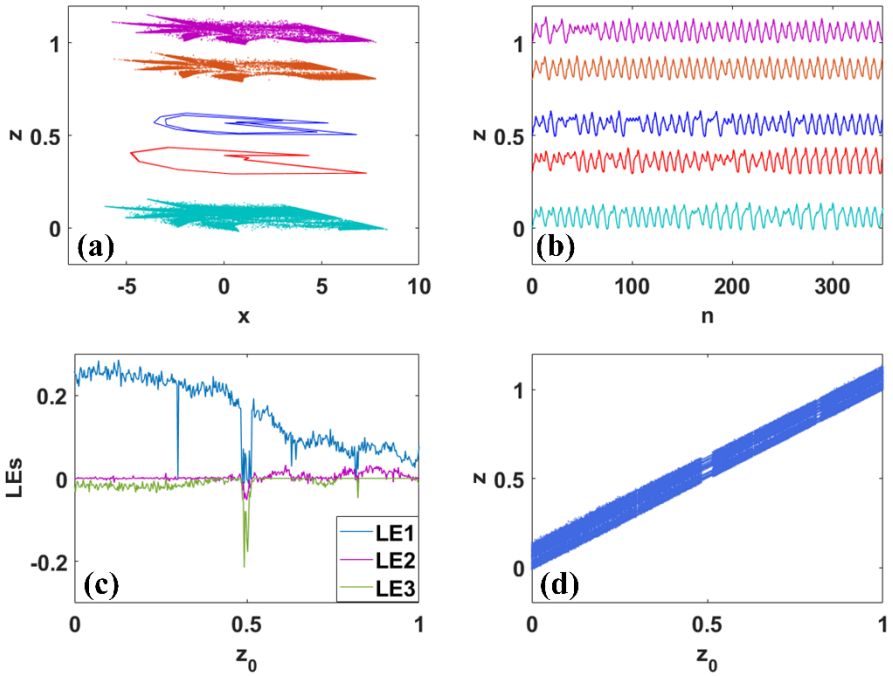

Fig. 4. Firing multistability of the map (2) in the x-z plane with $a = 8$, $b = 0.1$, $c = –0.4$ under $(x_0, y_0, z_0) = (1, 0, z_0)$, where turquoise: $z_0 = 0$, red: $z_0 = 0.3$, blue: $z_0 = 0.5$, chocolate: $z_0 = 0.8$, violet-red: $z_0 = 1$, (a) phase orbits, (b) signal sequences, (c) Lyapunov exponents, (d) bifurcation diagram.

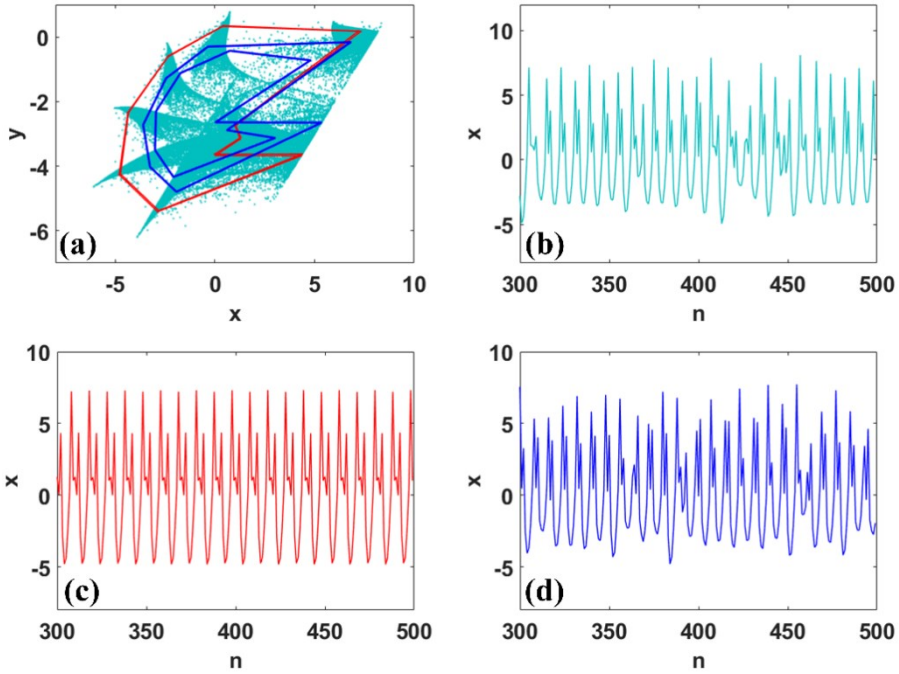

Fig. 5. Coexisting firings of the map (2) in the x-y plane with $a = 8$, $b = 0.1$, $c = –0.4$ under $(x_0, y_0, z_0) = (1, 0, z_0)$, where turquoise: $z_0 = 0$, red: $z_0 = 0.3$, blue: $z_0 = 0.5$, (a) phase orbits, (b) discrete sequences with $z_0 = 0$, (c) discrete sequences with $z_0 = 0.3$, (d) discrete sequences with $z_0 = 0.5$.

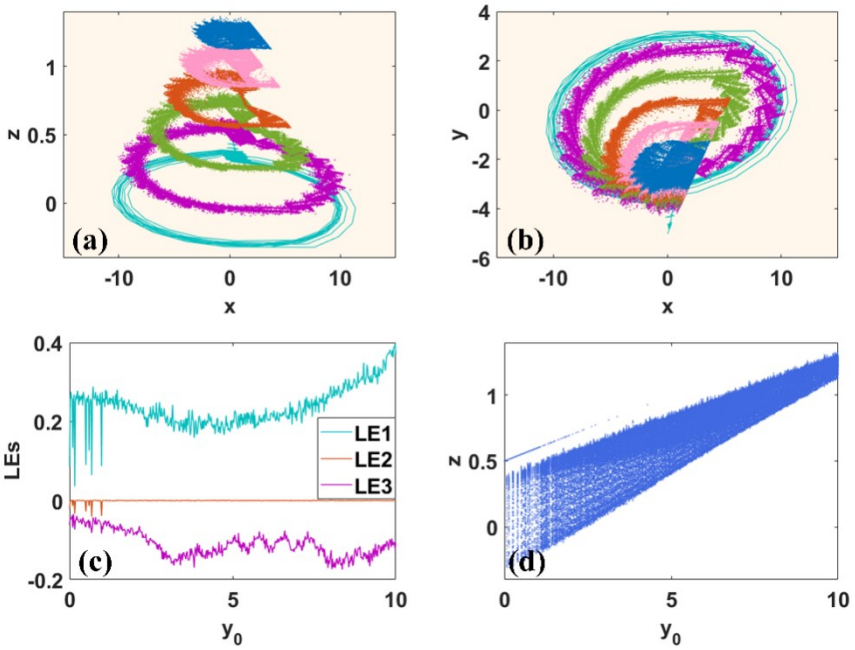

Fig. 6. Coexisting firings of the map (2) with $a = 5$, $b = 0.9$, $c = –0.1$ under $(x_0, y_0, z_0) = (1, y_0, 0)$, where turquoise: $y_0 = 0$, violet-red: $y_0 = 2$, green: $y_0 = 4$, chocolate: $y_0 = 6$, pink: $y_0 = 8$, sky blue: $y_0 = 10$: (a) x-z plane, (b) x-y plane, (c) Lyapunov exponents, (d) bifurcation diagram.

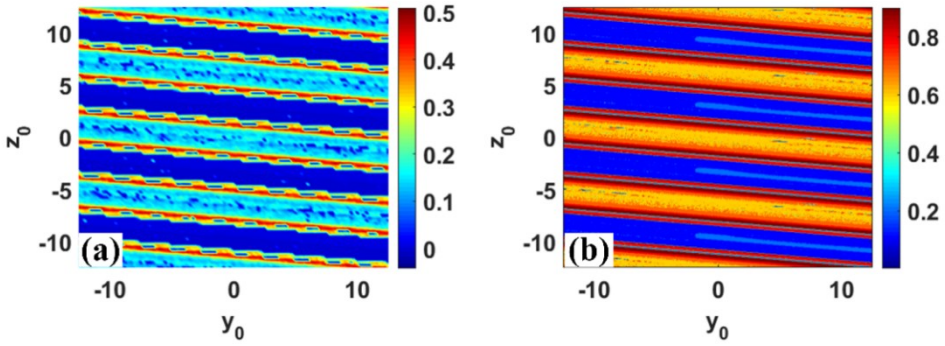

Fig. 7. The 2D Lyapunov exponents and sample entropy of the map (2) with $a = 5$, $b = 0.9$, $c = -0.1$ under $(x_0, y_0, z_0) = (1, y_0, z_0)$, when y_0, z_0 varies in $[-12.5, 12.5]$: (a) sample entropy, (b) Maximum Lyapunov exponent.

3. CH32-Based circuit implementation

Digital circuits implemented on CH32 have several advantages over analog circuits for implementing chaotic maps [24-26]. Firstly, CH32 microcontrollers perform calculations at a much faster rate than analog circuits, allowing for a more rapid generation of chaotic signals. Additionally, digital circuits are much easier to modify, which allows for greater flexibility in adjusting system parameters to create different types of chaos. Finally, digital circuits can be implemented using lower-cost components, which makes them more accessible to a wider range of users. As a result of these advantages, digital circuits implemented on CH32V307 are becoming increasingly popular for implementing chaotic maps in various applications. The procedure of signal processing in CH32V307 is displayed in Fig. 8.

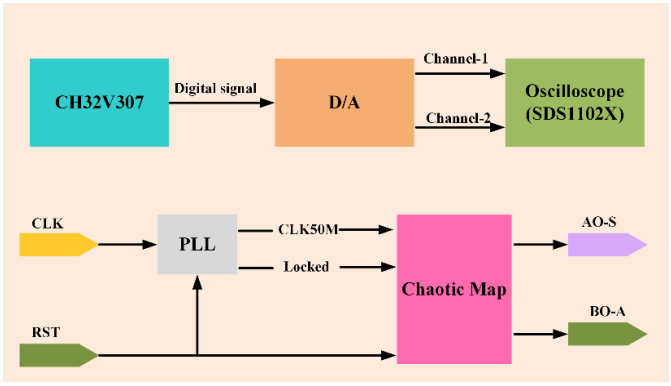

Fig. 8. The process of CH32-Based circuit implementation.

The calculation and output of chaotic mapping are implemented using a CH32V307 microcontroller, which is based on a 32-bit RISC-V instruction set and architecture.

With a maximum clock frequency of 144MHz, it features 256KB of Flash and 64KB of SRAM, and supports hardware floating-point arithmetic, greatly improving the speed of floating-point calculations, and making the calculation speed sufficient for mapping. Additionally, CH32V307 comes with 2 sets of 12-bit DACs for converting the chaotic digital signal into an analog voltage output, which can be displayed on an oscilloscope to show the phase trajectories. The platform for implementing hardware circuits is shown in Fig. 9. The features of firing multistability with $a = 5$, $b = 0.9$, $c = -0.1$ under $(x_0, y_0, z_0) = (1, y_0, 0)$, observed from the CH32-based circuit, are shown in Fig. 10, where violet-red: $y_0 = 2$, green: $y_0 = 4$, chocolate: $y_0 = 6$, pink: $y_0 = 8$, sky blue: $y_0 = 10$. Typical neuronal oscillations with $(x_0, y_0, z_0) = (1, 0, 0)$, implemented by digital circuits, are shown in Fig. 11, where (a)-(b) $a = 6$, $b = 0.1$, $c = -0.4$; for (c)-(d) $a = 8$, $b = 0.1$, $c = -0.4$; for (e)-(f) $a = 5$, $b = 0.8$, $c = -0.1$; for (g)-(h) $a = 5$, $b = 0.9$, $c = -0.1$.

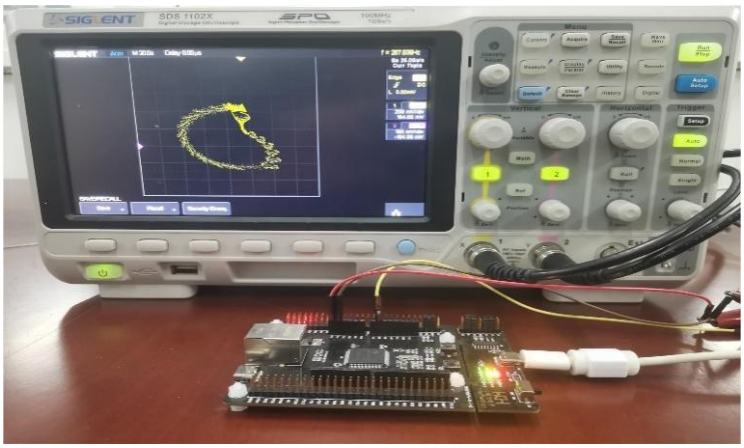

Fig. 9. The circuit output for the system (2) with $a = 5$, $b = 0.8$, $c = -0.1$.

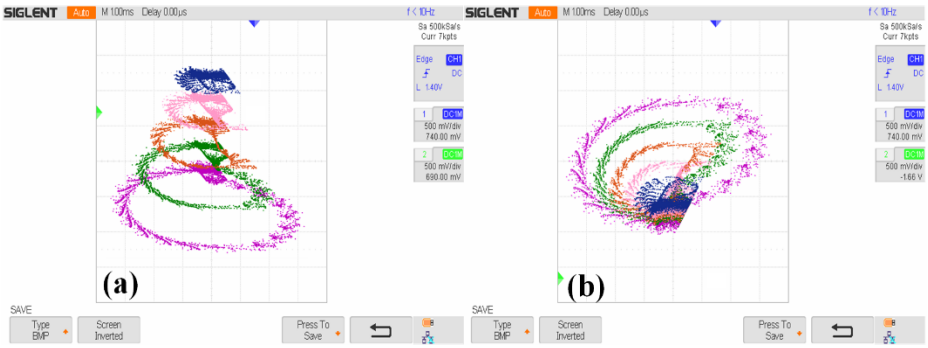

Fig. 10. Coexisting firings realized in the CH32-based circuit for the system (2) with $a = 5$, $b = 0.9$, $c = -0.1$ and $(x_0, y_0, z_0) = (1, 0, z_0)$: (a) x-z plane, (b) x-y plane. Here turquoise: $y_0 = 0$, violet-red: $y_0 = 2$, green: $y_0 = 4$, chocolate: $y_0 = 6$, pink: $y_0 = 8$, sky blue: $y_0 = 10$.

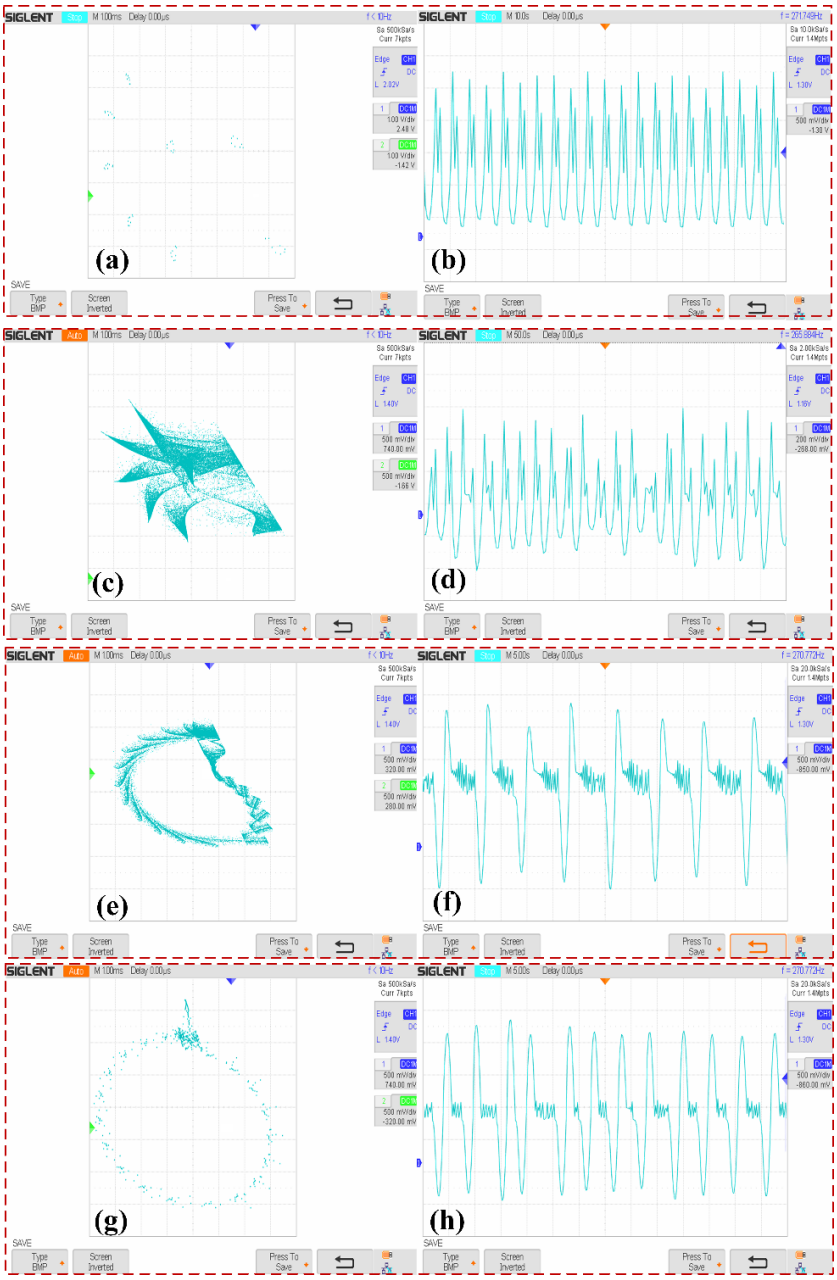

Fig. 11. Typical firings realized in the CH32-based circuit for the system (2) with (x_0, y_0, z_0) = (1, 0, 0) : (a)-(b) periodic spiking with a = 6, b = 0.1, c = –0.4, (c)-(d) chaotic spiking with a = 8, b = 0.1, c = –0.4, (e)-(f) chaotic bursting with a = 5, b = 0.8, c = –0.1, (g)-(h) periodic bursting with a = 5, b = 0.9, c = –0.1.

4. Application to image encryption

Within the framework of DMP, an essential formulation is introduced to demonstrate incremental and decremental updates for the inverse inner product and coefficient matrix. These matrices are employed by DMP to minimize the computational expense associated with variations in residual error, ultimately leading to a reduction in

computational complexity. In pursuit of heightened reconstruction accuracy and an expanded sparsity range for the reconstructed sparse signal, DMP adopts the assumption of sequential optimal reduction, followed by sequential optimal expansion of the support set elements. The assumed initial support set S is obtained by the DMP algorithm through the iterative minimization of the residual error Δ_s. Then, the given support set is iteratively updated through a process of reduction and expansion. These processes continue until Δ_s equals 0 or Δ_s is less than a specified tolerance value *tol*. At that point, the reduction and expansion process is terminated, and the correct support set S^* and sparse signal x are outputted. In Table. 2, Ψ refers to the measurement matrix, while N and K are the dimensions of the matrix.

Table 2. Pseudocode of DMP algorithm.

Algorithm 1 DMP

Input: $\boldsymbol{\Psi}$, $\boldsymbol{N}$, $\boldsymbol{K}$, ***tol***

Output: $\boldsymbol{S}$, $\boldsymbol{x}$

function DSMP($\boldsymbol{\Psi}$, $\boldsymbol{N}$, $\boldsymbol{K}$, ***tol***)

init: $S = \emptyset$; $\bar{S} = \Omega$; $\boldsymbol{C}_S = \emptyset$; $\boldsymbol{x} = 0$.

for $t = 1{:}K$

$i = \underset{i \in \bar{S}}{\operatorname{argmax}}(\Delta s - \Delta[S, i])$; $\boldsymbol{C}_S = \boldsymbol{C}_{[S,\, i]}$; $S = [S, i]$; $\bar{S} = \bar{S}/\{i\}$;

end for;

If $\Delta_s < tol$;

$x(S) = \boldsymbol{C}_S(\wedge, end)$;

reture;

end if;

$\boldsymbol{P}_S = \boldsymbol{\Psi}(S, S)^{-1}$; $b = 0$;

while $b < \boldsymbol{K}$-1;

$b = b + 1$; $\omega_b = \underset{\omega_b \in S/\{\omega_1, .., \omega_{b-1}\}}{\operatorname{argmax}} (\Delta_{S/\{\omega 1, \ldots, \omega b\}} - \Delta_{S/\{\omega 1, \ldots, \omega b\}})$; $\boldsymbol{P}_{S/\{\omega 1, \ldots, \omega b\}}$; $\boldsymbol{C}_{S/\{\omega 1, \ldots, \omega b\}}$;

if $S/\{\omega_1, \ldots, \omega_b\} = S(1{:}\boldsymbol{K}\text{-}b)$;

continue; end if;

for $t = b{:}\text{-}1{:}1$

if $\{\omega_b, \ldots, \omega_t\} \cup \{v_b, \ldots, v_t\} = \{\omega_b, \ldots, \omega_t\}$; $t = 0$; break; end; if

$\boldsymbol{P}_{[S/\{\omega 1, \ldots, \omega b\}, vb, \ldots, vI]}$; $\boldsymbol{C}_{[S/\{\omega 1, \ldots, \omega b\}, vb, \ldots, vI]}$;

$v_t = \underset{v_t \in [\omega_b, .., \omega_1 \bar{S}/\{v_b, .., v_{t+1}\}]}{\operatorname{argmax}} (\Delta_{[S/\{\omega_1, \ldots, \omega_b\}, v_b, \ldots, v_{t+1}]} - \Delta_{[S/\{\omega_1, \ldots, \omega_b\}, v_b, \ldots, v_t]})$

end for

if $t = 0$; continue; end if;

if $\Delta_{[S/\{\omega 1, \ldots, \omega b\}, vb, \ldots, vI]} \geq \Delta_S$;

continue; end if;

$S = [S/\{\omega_1, \ldots, \omega_b\}, v_b, \ldots, v_1]$; $\bar{S} = [\bar{S}/\{\omega_1, \ldots, \omega_b\}, v_b, \ldots, v_1]$

$\boldsymbol{P}_{[S/\{\omega 1,\ldots,\omega b\},vb,\ldots,vI]}$; $\boldsymbol{C}_{[S/\{\omega 1,\ldots,\omega b\},vb,\ldots,vI]}$; $b = 0$
if $\Delta_S < tol$;
break; end if;
end while
end function

Algebraic operations are designed by leveraging the four nucleotide pairing modes of DNA in DNA coding operations. By converting binary data into a DNA-encoded form, operations such as addition, subtraction, and XOR can be performed, facilitating the encryption of digital signals. In DNA systems, extensive variations in image data can be achieved through a single round of DNA coding and decoding, making it suitable for the design of encryption algorithms. A color chaotic image encryption algorithm, based on the combination of DMP compressive sensing and DNA coding, is proposed in this paper. The utilization of the DMP compressive sensing algorithm enables image compression and reconstruction in the wavelet domain. The generation of the required measurement matrix for the compressive sensing algorithm involves utilizing a three-dimensional chaotic system, and a 4-column chaotic sequence is generated for the DNA encryption algorithm. A higher level of randomness is introduced in the encryption process, resulting in effective encryption. The computational flowchart of the encryption algorithm is illustrated in Fig. 12.

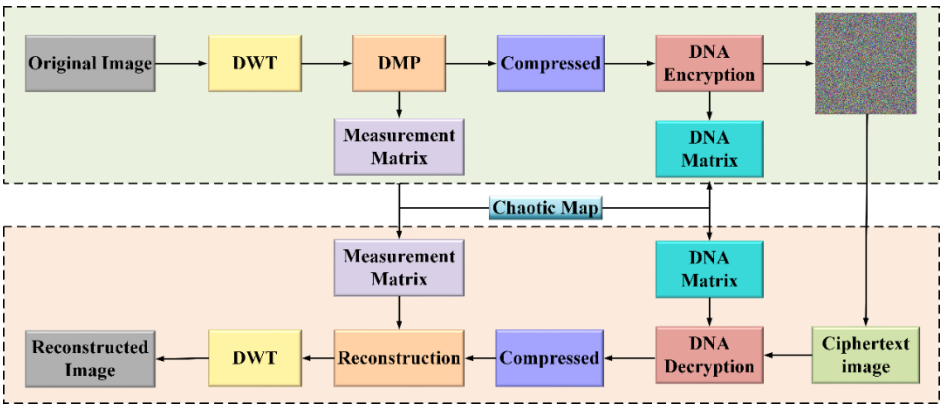

Fig. 12. Algorithm architecture.

In order to resist brute-force attacks, it is necessary for the key space of an algorithm to be sufficiently large. The encryption algorithm proposed in this paper employs the initial values and parameters of the chaotic system, specifically x, y, z, a, b, and c, as secret keys to achieve this. The precision of the initial values x_0, y_0, z_0 is 1×10^{-15}, and the precision of the parameters a, b, and c is 1×10^{-15}, 1×10^{-16}, and 1×10^{-17}, respectively. Hence, it can be ascertained that the key space of this algorithm is determined by the following parameters: $(1 \times 10^{-15} \times 1 \times 10^{-15} \times 1 \times 10^{-15} \times 1 \times 10^{-15} \times 1 \times 10^{-16}\ 1 \times 10^{-17})^{-1}$. When the original image is 128 × 256, the key space of the

original image is $128 \times 256 \times 2^8 = 1.3 \times 2^{22}$. The total keyspace value can reach 1.3×2^{241}. The obtained key-value satisfies the security requirements of a keyspace with more than 100 bits. In the chaotic image encryption algorithm, the chaotic map is introduced simultaneously with the compressive sensing and encryption algorithms [27-29]. In this case, when an algorithm is subjected to a brute-force attack by an attacker, the key information of the chaotic system not only causes decryption failure but also leads to reconstruction failure in compressive sensing. The keys are $x_0 = 1$, $y_0 = 0$, $z_0 = 1$, $a = 8$, $b = 0.1$, $c = -0.4$. Key sensitivity tests are performed based on these parameters. As illustrated in Fig. 13, during the standard image decryption process, decryption fails when x_0 is changed to $1 + 1 \times 10^{-15}$, when y_0 is changed to $0 + 1 \times 10^{-15}$; z_0 is changed to $1 + 1 \times 10^{-15}$; when a is changed to $8 + 1 \times 10^{-15}$; when b is changed to $0.1 + 1 \times 10^{-16}$; and when c is changed to $-0.4 + 1 \times 10^{-17}$. Similarly, the results of compressive sensing reconstruction are shown in Fig. 13(b).

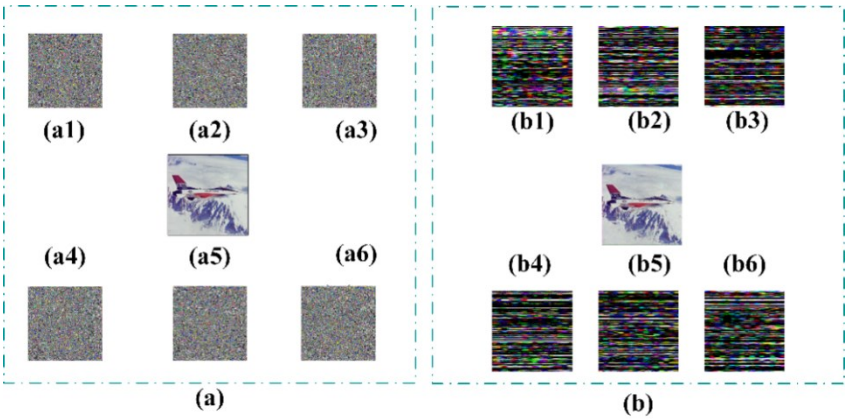

Fig. 13. (a) Image of key sensitivity, where (a1) $x_0 + 1\times10^{-15}$, (a2) $y_0 + 1\times10^{-15}$, (a3) $z_0 + 1\times10^{-15}$, (a4) $a + 1\times10^{-15}$, (a5) $b + 1\times10^{-16}$, (a6) $c + 1\times10^{-17}$, (b) Image of compressed sensing matrix, where (b1) $x_0 + 1\times10^{-15}$, (b2) $y_0 + 1\times10^{-15}$, (b3) $z_0 + 1\times10^{-15}$, (b4) $a + 1\times10^{-15}$, (b5) $b + 1\times10^{-16}$, (b6) $c + 1\times10^{-17}$.

In phase space, attractors with the same shape and state but located at different locations are referred to as homogeneous multistability [30-32]. Coexisting attractors with different shapes are called heterogeneous multistability. Coexisting homogeneous and heterogeneous multistability brings greater key space and more encryption channels to image encryption. As displayed in Fig. 4, when $a = 8$, $b = 0.1$, $c = -0.4$ under $(x_0, y_0, z_0) = (1, 0, z_0)$, and for $z_0 = 0$, 0.8, 1, there is homogeneous multistability. Here the initial conditions z_0 are selected as 0.5, 0.8, and 1 respectively to explore the encryption performance of homogeneous and heterogeneous multistability. The image is reconstructed successfully at $z_0 = 0.8$ and 1, but when $z_0 = 0.5$, the image is reconstructed failed with the periodic attractor. The encryption influence of coexisting attractors is plotted in Fig. 14, where for (a1)-(f1): $z_0 = 0.5$, for (a2)-(f2): $z_0 = 0.8$, for (a3)-(f3): $z_0 = 1$. Multiple metrics are subjected to testing, including Near Pixel Change

Rate (NPCR), Unified Average Changing Intensity (UACI), information entropy, etc. The results demonstrated that the homogeneous multistability of chaotic attractors exhibited similar performance. When solutions are chaotic, the performance of the encryption algorithm closely approximated the ideal values for each metric, whereas in the case of periodic attractors, there was a significant deviation from the ideal values.

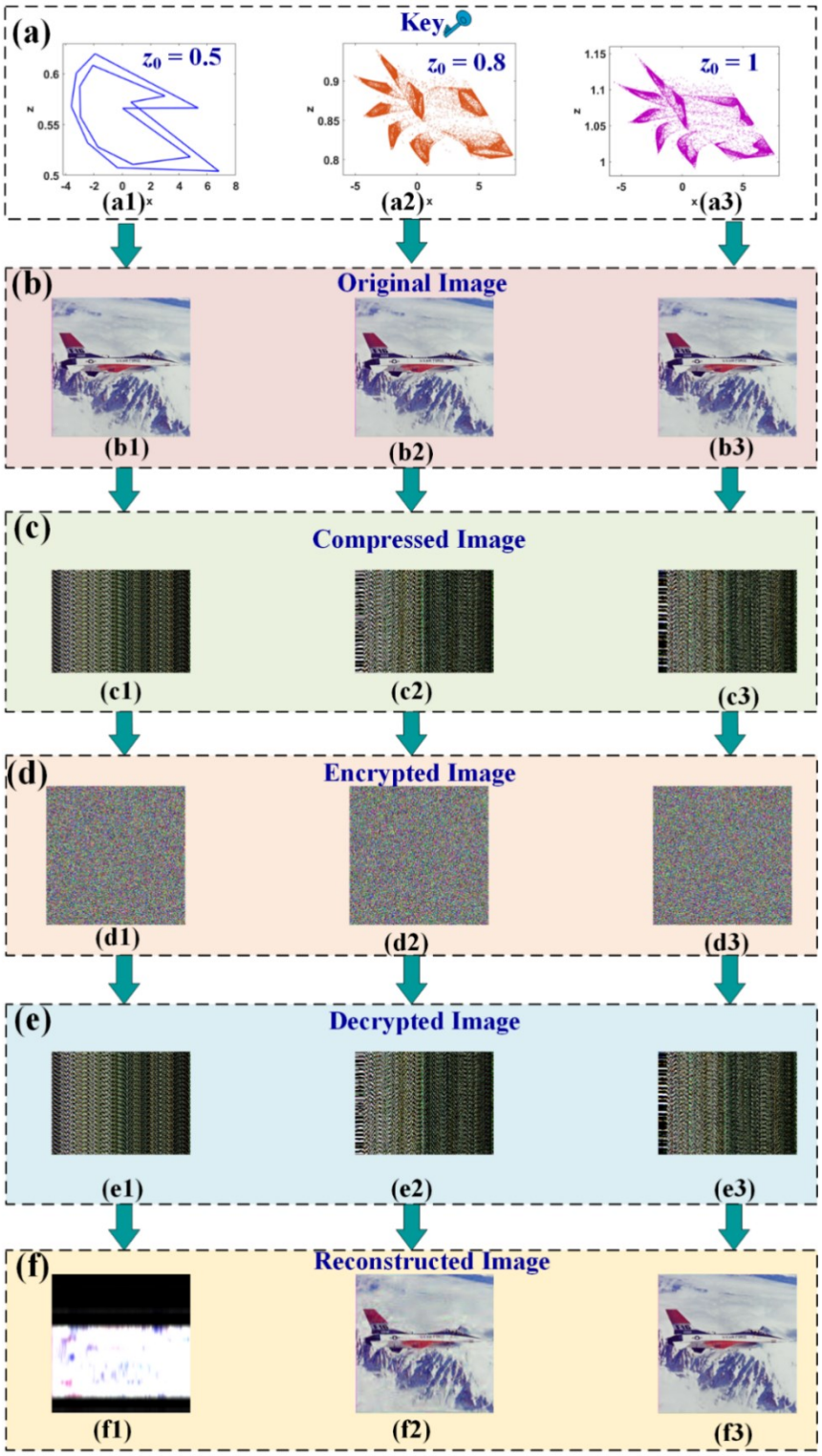

Fig. 14. The encryption influence of coexisting attractors with $a = 8$, $b = 0.1$, $c = –0.4$ under $(x_0, y_0, z_0) = (1, 0, z_0)$: (a) typical neuronal oscillation, (b) original image, (c) compressed image, (d) encrypted image, (e) decrypted image, (f) reconstructed image.

In the encryption algorithm, effective resistance against differential attacks can be inferred when the Near Pixel Change Rate (NPCR) approaches 99.6094% and the Unified Average Changing Intensity (UACI) approaches 33.4635%. The formulae for NPCR and UACI can be derived from the following Eqs. (3)-(4). Stronger resistance against differential attacks is indicated by higher values of NPCR and UACI in the encryption algorithm. NPCR and UACI values are depicted in Table. 3 with different initial conditions. The correlation between adjacent pixels of plaintext and ciphertext is presented in Table 4.

$$NPCR = \frac{\sum_{i,j} D(i,j)}{MN} 100\% \tag{3}$$

$$UACI = \frac{1}{M \times N} \frac{\sum (C_1(i,j) - C_2(i,j))}{255} 100\% \tag{4}$$

Table 3. NPCR and UACI values with $a = 8$, $b = 0.1$, $c = –0.4$ under $(x_0, y_0, z_0) = (1, 0, z_0)$.

NPCR and UACI		
IC	NPCR	UACI
$z_0 = 0.5$	99.6399	31.7470
$z_0 = 0.8$	99.6155	33.2200
$z_0 = 1.0$	99.6170	33.2590

In general images, a high correlation exists between adjacent pixels, rendering textual and graphic content susceptible to statistical attacks. Therefore, analyzing the encryption effectiveness of an image by evaluating the correlation coefficient between adjacent pixels holds value. The correlation between adjacent pixels can be calculated using the following Eqs. (5)-(7). The correlation between adjacent pixels is displayed in Fig. 15.

$$r_{xy} = \frac{\mathrm{cov}(x,y)}{\sqrt{D(x)}\sqrt{D(y)}}, \tag{5}$$

$$\mathrm{cov}(x,y) = \frac{1}{N} \sum_{i=1}^{N} (x_i - E(x))(y_i - E(y)), \tag{6}$$

$$D(x)=\frac{1}{N}\sum_{i=1}^{N}(x_i-E(x))^2, E(x)=\frac{1}{N}\sum_{i=1}^{N}x_i. \quad (7)$$

Table 4. Correlation between adjacent pixels of plaintext and ciphertext.

IC		Compressed Image			Encrypted Image		
		Horizontal	Vertical	Diagonal	Horizontal	Vertical	Diagonal
$z_0 = 0.5$	R	-0.0581	0.3358	-0.1254	-0.0121	0.0129	0.0123
	G	-0.0168	0.3168	-0.0939	0.0124	-0.0116	0.0168
	B	-0.0405	0.3134	-0.0753	-0.0262	-0.0103	-0.0183
$z_0 = 0.8$	R	0.0221	0.2572	0.0047	0.0019	-0.0092	0.0034
	G	-0.0122	0.2423	-0.0422	-0.0055	0.0036	-0.0047
	B	0.0372	0.2575	0.0437	-0.0031	0.0035	-0.0049
$z_0 = 1$	R	0.0493	0.1818	-0.1001	-0.0035	0.0031	-0.0037
	G	0.0525	0.1704	-0.10878	-0.0025	0.0045	0.0056
	B	0.0884	0.2149	-0.0101	0.0073	0.0075	0.0039

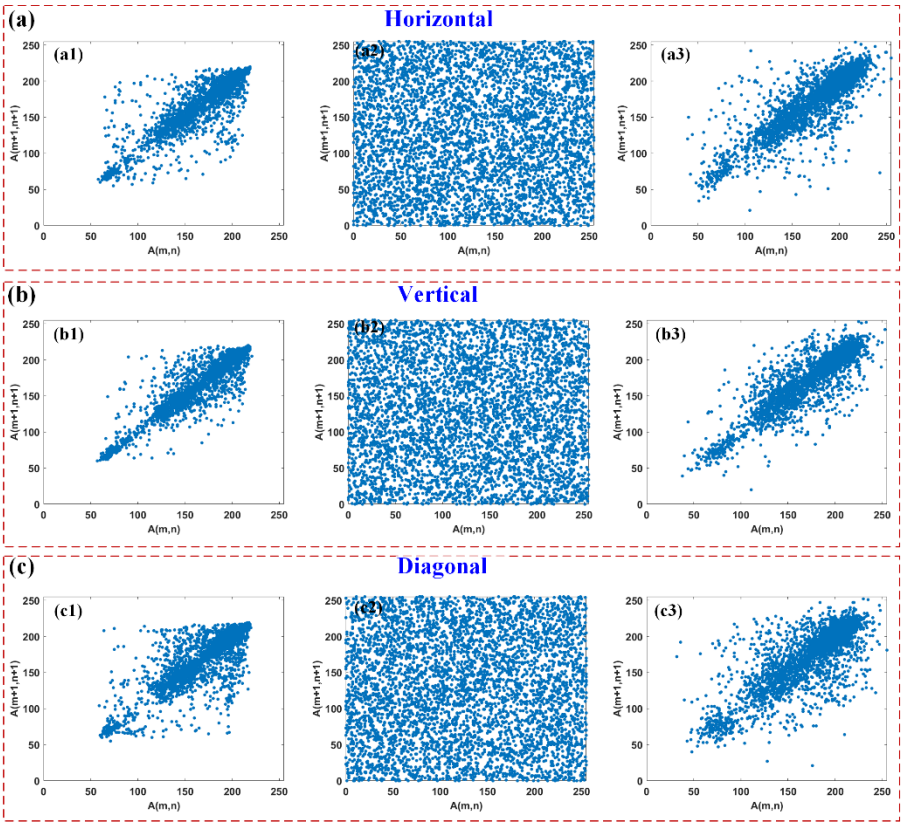

Fig. 15. Correlation between adjacent pixels with $a = 8$, $b = 0.1$, $c = -0.4$ under $(x_0, y_0, z_0) = (1, 0, 1)$ in R channel: where (a1)-(c1) plaintext, (a2)-(c2) ciphertext, (a3)-(c3) degrade plaintext.

How the pixels are distributed and whether the encryption algorithm effectively resists statistical analysis can be determined by examining the histogram of an image. If the pixel distribution in the encrypted image is non-uniform, partial statistical information can be obtained by attackers through the utilization of statistical analysis. Therefore, great value is held by histogram distribution in cryptographic analysis. The histogram of the encrypted image is plotted in Fig. 16.

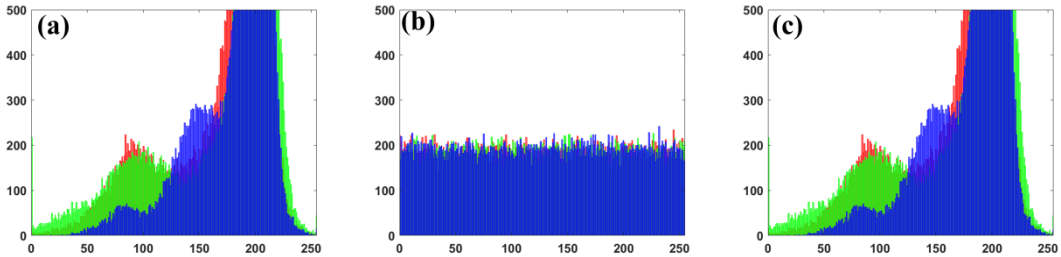

Fig. 16. Histogram image of R, G, B channel in Airplane with $a = 8$, $b = 0.1$, $c = -0.4$ under $(x_0, y_0, z_0) = (1, 0, 1)$: (a) original image, (b) encrypted image, (c) observation image.

The entropy of information, which quantifies the randomness of data, can be calculated using Eq. (8). The encryption effectiveness of the technique is stronger and the probability of data leakage is lower when the entropy value approaches 8 [33-35]. The entropy of the three channels of the image is presented in Table 5.

$$H(m) = \sum_{i=0}^{2^n-1} p(m_i) \log_2 \frac{1}{p(m_i)} \tag{8}$$

Table 5. Information entropy of cipher.

IC		Compressed Image	Encrypted Image
$z_0 = 0.5$	R	3.7950	7.9959
	G	3.7627	7.9961
	B	3.8449	7.9961
$z_0 = 0.8$	R	4.2223	7.9969
	G	4.0949	7.9977
	B	4.2228	7.9970
$z_0 = 1.0$	R	4.2214	7.9973
	G	4.0867	7.9974
	B	4.2189	7.9970

6. Conclusion

In this work, the incorporation of discrete memristors into the Rulkov neuron has effectively showcased the emergence of rich brain-like dynamics. Notably, the memristor-related parameter has proven to be instrumental in transitioning between periodic spiking, chaotic spiking, and chaotic bursting activities. Additionally, the capacity of the memristor to regulate coexisting homogeneous and heterogeneous multistability has been substantiated through an examination involving Lyapunov exponents, discrete sequences, and sample entropy. Furthermore, the encryption capabilities of homogeneous and heterogeneous multistability have been unveiled through a novel approach that combines DMP and DNA coding. This research bolsters the confidence in the potential of chaotic maps as a promising avenue for enhancing information encryption, ultimately bridging the gap between low security associated with periodic signals and the heightened security afforded by chaotic signals [36-39].

Data availability statement

The data that support the findings of this study are available from the corresponding author upon reasonable request.

CRediT authorship contribution statement

Yongxin Li: Investigation, Software, Visualization, Circuit simulation, Data curation, Writing - original draft. **Chunbiao Li:** Conceptualization, Methodology, Writing-review & editing, Project administration, Funding acquisition. **Yaning Li:** Validation, Circuit implementation. **Irene Moroz:** Validation, Visualization. **Yong Yang:** Validation, Investigation, Resources.

Acknowledgments

This work was supported financially by the National Natural Science Foundation of China (Grant No.: 62371242), and a project funded by the Priority Academic Program Development of Jiangsu Higher Education Institutions.

Conflict of interest

We declare that we have no known competing financial interests or personal relationships that could have appeared to influence the work reported in this paper.

References

[1] Lin H, Wang C, Du S, et al. A family of memristive multibutterfly chaotic systems with multidirectional initial-based offset boosting. Chaos, Solitons & Fractals, 2023, 172: 113518.

[2] Díaz E A H, Meana H M P, García V M S. Encryption of RGB images by means of a novel cryptosystem using elliptic curves and chaos. IEEE Latin America Transactions, 2020, 18(08): 1407-1415.

[3] Yu L, Barbot J P, Zheng G, et al. Compressive sensing with chaotic sequence. IEEE Signal Processing Letters, 2010, 17(8): 731-734.

[4] Yang F, An X. A new discrete chaotic map application in image encryption algorithm. Physica Scripta, 2022, 97(3): 035202.

[5] Wang S, Wei Z. Synchronization of coupled memristive Hindmarsh–Rose maps under different

coupling conditions. AEU-International Journal of Electronics and Communications, 2023, 161: 154561.
[6] Innocenti G, Morelli A, Genesio R, et al. Dynamical phases of the Hindmarsh-Rose neuronal model: Studies of the transition from bursting to spiking chaos. Chaos: An Interdisciplinary Journal of Nonlinear Science, 2007, 17(4): 043128.
[7] Lakshmanan S, Lim C P, Nahavandi S, et al. Dynamical analysis of the Hindmarsh–Rose neuron with time delays. IEEE transactions on neural networks and learning systems, 2016, 28(8): 1953-1958.
[8] Hodgkin A L, Huxley A F. Currents carried by sodium and potassium ions through the membrane of the giant axon of Loligo. The Journal of Physiology, 1952, 116(4): 449.
[9] Kuptsov P V, Stankevich N V, Bagautdinova E R. Discovering dynamical features of Hodgkin–Huxley-type model of physiological neuron using artificial neural network. Chaos, Solitons & Fractals, 2023, 167: 113027.
[10] FitzHugh R. Impulses and physiological states in theoretical models of nerve membrane. Biophysical journal, 1961, 1(6): 445-466.
[11] Njitacke Z T, Ramadoss J, Takembo C N, et al. An enhanced FitzHugh–Nagumo neuron circuit, microcontroller-based hardware implementation: Light illumination and magnetic field effects on information patterns. Chaos, Solitons & Fractals, 2023, 167: 113014.
[12] Chua L. Memristor-the missing circuit element. IEEE Transactions on Circuit Theory, 1971, 18(5): 507-519.
[13] Strukov D B, Snider G S, Stewart D R, et al. The missing memristor found. Nature, 2008, 453(7191): 80-83.
[14] Babacan Y, Kaçar F, Gürkan K. A spiking and bursting neuron circuit based on memristor. Neurocomputing, 2016, 203: 86-91.
[15] Li Z, Peng C, Wang M, et al. Dynamic behavior in memristor coupled Hindmarsh–Rose and Fitzhugh–Nagumo neurons with synaptic crosstalk. Indian Journal of Physics, 2023: 1-17.
[16] Zhang S, Li C, Zheng J, et al. Memristive Autapse-Coupled Neuron Model With External Electromagnetic Radiation Effects. IEEE Transactions on Industrial Electronics, 2022.
[17] Bao H, Hua Z, Li H, et al. Discrete memristor hyperchaotic maps. IEEE Transactions on Circuits and Systems I: Regular Papers, 2021, 68(11): 4534-4544.
[18] Li H, Hua Z, Bao H, et al. Two-dimensional memristive hyperchaotic maps and application in secure communication. IEEE transactions on industrial electronics, 2020, 68(10): 9931-9940.
[19] Li K, Bao H, Li H, et al. Memristive Rulkov neuron model with magnetic induction effects. IEEE Transactions on Industrial Informatics, 2021, 18(3): 1726-1736.
[20] Ma M, Lu Y, Li Z, et al. Multistability and phase synchronization of Rulkov neurons coupled

with a locally active discrete memristor. Fractal and Fractional, 2023, 7(1): 82.
[21] Li Y, Li C, Zhang S, et al. A self-reproduction hyperchaotic map with compound lattice dynamics. IEEE Transactions on Industrial Electronics, 2022, 69(10): 10564-10572.
[22] Li Y, Li C, Zhong Q, et al. A memristive chaotic map with only one bifurcation parameter. Nonlinear Dynamics, 2024: 1-18.
[23] Bao H, Li K X, Ma J, et al. Memristive effects on an improved discrete Rulkov neuron model. Science China Technological Sciences, 2023: 1-11.
[24] Li Z, Yi Z. A memristor‐based associative memory circuit considering synaptic crosstalk. Electronics Letters, 2022, 58(14): 539-541.
[25] He S, Fu L, Lu Y, et al. Analog circuit of a simplified Tent map and its application in sensor position optimization. IEEE Transactions on Circuits and Systems II: Express Briefs, 2022.
[26] Vaidyanathan S, Sambas A, Tlelo-Cuautle E, et al. A new 4-D multi-stable hyperchaotic system with no balance point: Bifurcation analysis, circuit simulation, FPGA realization and image cryptosystem. IEEE Access, 2021, 9: 144555-144573.
[27] Yuan F, Zhang S, Xing G, et al. Parameter Control Methods for Discrete Memristive Maps with Network Structure. IEEE Transactions on Industrial Informatics, 2024.
[28] Zhang S, Li C, Zheng J, et al. Generating any number of initial offset-boosted coexisting Chua's double-scroll attractors via piecewise-nonlinear memristor. IEEE Transactions on Industrial Electronics, 2021, 69(7): 7202-7212.
[29] Vivekanandhan G, Natiq H, Ghaffari A, et al. A new chaotic jerk system with hidden heart-shaped attractor: dynamical analysis, multistability, connecting curves and its application in image encryption. Physica Scripta, 2023, 98(11): 115207.
[30] Yuan F, Li S, Deng Y, et al. Cu-Doped TiO_2 Nanoscale Memristive Applications in Chaotic Circuit and True Random Number Generator. IEEE Transactions on Industrial Electronics, 2022, 70(4): 4120-4127.
[31] Yang F, Xu Y, Ma J. A memristive neuron and its adaptability to external electric field. Chaos: An Interdisciplinary Journal of Nonlinear Science, 2023, 33(2).
[32] Li Y, Li C, Lei T, et al. Offset Boosting-Entangled Complex Dynamics in the Memristive Rulkov Neuron. IEEE Transactions on Industrial Electronics, 2023.
[33] Sriram B, Ghaffari A, Rajagopal K, et al. A chaotic map with trigonometric functions: Dynamical analysis and its application in image encryption based on sparse representation and convolutional filters. Optik, 2023, 273: 170379.
[34] Li Y, Li C, Zhong Q, et al. Coexisting hollow chaotic attractors within a steep parameter interval. Chaos, Solitons & Fractals, 2024, 179: 114406.
[35] Yao W, Liu J, Sun Y, et al. Dynamics analysis and image encryption application of Hopfield

neural network with a novel multistable and highly tunable memristor. Nonlinear Dynamics, 2024, 112(1): 693-708.

[36] Liu W, Sun K, He S, et al. The Parallel Chaotification Map and Its Application. IEEE Transactions on Circuits and Systems I: Regular Papers, 2023.

[37] Zhang S, Zhang H, Wang C. Dynamical analysis and applications of a novel 2-D hybrid dual-memristor hyperchaotic map with complexity enhancement. Nonlinear Dynamics, 2023: 1-27.

[38] Meucci R, Marc Ginoux J, Mehrabbeik M, et al. Generalized multistability and its control in a laser. Chaos: An Interdisciplinary Journal of Nonlinear Science, 2022, 32(8).

[39] Minati L, Gambuzza L V, Thio W J, et al. A chaotic circuit based on a physical memristor. Chaos, Solitons & Fractals, 2020, 138: 109990.